

Codesigning Alloy Compositions of $\text{CdSe}_y\text{Te}_{1-y}$ Absorbers and $\text{Mg}_x\text{Zn}_{1-x}\text{O}$ Contacts to Increase Solar Cell Efficiency

Imran S. Khan, Tursun Ablekim, Deborah L. McGott, Brian Good, Craig L. Perkins, Wyatt K. Metzger, and Andriy Zakutayev*

Thin-film solar cells such as CdTe are a major commercial photovoltaic technology, with more than 25 GW installed worldwide and leveled costs of electricity competitive with fossil fuels. Further progress may result from integrating $\text{CdSe}_y\text{Te}_{1-y}$ absorbers with $\text{Mg}_x\text{Zn}_{1-x}\text{O}$ contacts, but the device efficiency is difficult to maximize due to coupled dependence on chemical composition of both alloys. Herein, a high-throughput approach is demonstrated to codesign chemical compositions in alloyed $\text{Mg}_x\text{Zn}_{1-x}\text{O}/\text{CdSe}_y\text{Te}_{1-y}$ thin-film solar cells, using combinatorial libraries of PV devices with orthogonal composition gradients in $\text{CdSe}_y\text{Te}_{1-y}$ absorbers and $\text{Mg}_x\text{Zn}_{1-x}\text{O}$ contacts. It is found that the solar cell performance is a strong and coupled function of both elemental compositions, with efficiency up to 17.7% ($V_{\text{OC}} = 836$ mV, fill factor = 69%, $J_{\text{SC}} = 30.6$ mA cm⁻²) at atomic compositions of $\text{Mg}/(\text{Mg} + \text{Zn}) \approx 18\%$ and average $\text{Se}/(\text{Se} + \text{Te}) \approx 4\%$. These performance trends among >100 devices are explained by >100 ns lifetime of photoexcited charge carriers at the $\text{Mg}_x\text{Zn}_{1-x}\text{O}/\text{CdSe}_y\text{Te}_{1-y}$ interface where strong Se accumulation is also observed. This study reports the optimal compositions of the commercially relevant $\text{Mg}_x\text{Zn}_{1-x}\text{O}/\text{CdSe}_y\text{Te}_{1-y}$ solar cells and demonstrates a general approach to codesigning performance of alloyed thin-film solar cells and other optoelectronic devices.

is still room for further improvement. One way this can be achieved is by alloying CdTe with CdSe to lower the absorber bandgap. The bandgap of $\text{CdSe}_y\text{Te}_{1-y}$ dilute alloys decreases with increasing Se content due to the bandgap bowing effect,^[3] which improves carrier collection resulting in increased short-circuit current (J_{SC}).^[4] Despite the $\text{CdSe}_y\text{Te}_{1-y}$ reduced absorber bandgap, the V_{OC} is sustained because Se addition improves carrier lifetime.^[5] The $\text{CdSe}_y\text{Te}_{1-y}$ alloys are often synthesized by subjecting a bilayer CdSe/CdTe to CdCl₂ treatment, whereupon the elements interdiffuse.

The integration of $\text{Mg}_x\text{Zn}_{1-x}\text{O}$ as a front contact has significantly increased efficiency in different PV technologies^[6] including CdTe.^[7] $\text{Mg}_x\text{Zn}_{1-x}\text{O}$ has a tunable bandgap and conduction band position as a function of Mg content,^[8] both higher than ZnO ($E_g = 3.24$ eV). There are varying reports on the $\text{Mg}_x\text{Zn}_{1-x}\text{O}$ band gap (4.0–4.2 eV) at maximum Mg composition ($x = 0.36$ – 0.46) at which phase


segregation occurs, as it depends on the deposition technique, deposition rate, and substrate temperature.^[8,9] $\text{Mg}_x\text{Zn}_{1-x}\text{O}$ has also been studied using different combinatorial methods, such as pulsed laser deposition,^[10] chemical vapor deposition,^[11] and sputtering,^[12] where we demonstrated $\text{Mg}_x\text{Zn}_{1-x}\text{O}$ conduction band tuning and integrated it with wide-bandgap CuGa_3Se_5 absorber to increase V_{OC} close to ≈ 1 V. The $\text{Mg}_x\text{Zn}_{1-x}\text{O}/\text{CdSe}_y\text{Te}_{1-y}$ device interface was also recently studied, demonstrating improvements in J_{SC} and efficiency due to widened bandgap and better carrier collection at low wavelengths.^[13]

Finding the optimum composition in $\text{Mg}_x\text{Zn}_{1-x}\text{O}$ and $\text{CdSe}_y\text{Te}_{1-y}$ is complicated as Mg in $\text{Mg}_x\text{Zn}_{1-x}\text{O}$ and Se in $\text{CdSe}_y\text{Te}_{1-y}$ both change the conduction band alignment and interface defect density, which can have significant impacts on interface recombination, barrier heights, and V_{OC} .^[14] Modeling studies^[7,15] may provide some insight into understanding experimental results, however often have limitations in predicting the future device performance. This coupled absorber/contact codesign problem can be addressed using high-throughput experimental (combinatorial) methods,^[16] by creating PV device libraries with orthogonal composition gradients in the $\text{CdSe}_y\text{Te}_{1-y}$ and $\text{Mg}_x\text{Zn}_{1-x}\text{O}$ layers. In the past, combinatorial methods have been used to study compositionally

1. Introduction

CdTe-based solar cells have become one of the leading photovoltaic (PV) technologies, with more than 25 GW worldwide installation, 37% of the USA utility-scale deployment in 2019, and laboratory cell efficiency reaching 22.1%.^[1] However, the Shockley–Queisser limit of 33%^[2] for single-junction CdTe (bandgap, $E_g = 1.5$ eV) devices suggests that there

I. S. Khan, T. Ablekim,^[†] D. L. McGott, B. Good, C. L. Perkins, W. K. Metzger,^[†] A. Zakutayev
National Renewable Energy Laboratory
Golden, CO 80401, USA
E-mail: andriy.zakutayev@nrel.gov

 The ORCID identification number(s) for the author(s) of this article can be found under <https://doi.org/10.1002/solr.202200394>.

^[†]Present address: First Solar, Perrysburg, OH 43551, USA

© 2022 The Authors. Solar RRL published by Wiley-VCH GmbH. This is an open access article under the terms of the Creative Commons Attribution-NonCommercial License, which permits use, distribution and reproduction in any medium, provided the original work is properly cited and is not used for commercial purposes.

DOI: 10.1002/solr.202200394

graded CdTe,^[17] CIGS,^[18] Cu₂ZnSnCh₄,^[19] CuSbCh₂,^[20] absorbers or Mg_xZn_{1-x}O,^[12] Zn-Ni-Co-O,^[21] Cu_xZn_{1-x}S,^[22] and CdS^[23] contacts in thin-film solar cells. However, the reports on codesign of absorbers and contacts are limited to early-stage development of all-oxide solar cells^[24] or organic PV.^[25] Applying such codesign approaches to commercially relevant inorganic chalcogenide solar cells is missing from literature.

Here, we codesign Mg_xZn_{1-x}O/CdSe_yTe_{1-y} solar cell performance by finding the optimum alloy compositions in Mg_xZn_{1-x}O contact and CdSe_yTe_{1-y} absorber layers. The bandgap tunability range for Mg_xZn_{1-x}O without forming secondary phases and Se accumulation at the CdSe_yTe_{1-y}/Mg_xZn_{1-x}O interface are shown. The device performance data facilitated identifying the optimal composition range for Mg_xZn_{1-x}O and CdSe_yTe_{1-y} at Mg/(Mg + Zn) ≈ 18% and average Se/(Se + Te) ≈ 4% respectively, which resulted in solar cell device with V_{OC} = 836 mV, fill factor = 69%, J_{SC} = 30.6 mA cm⁻² and efficiency up to 17.7%. The device performance trends are explained based on the changing contact/absorber bandgaps and increased charge carrier lifetimes at Mg_xZn_{1-x}O/CdSe_yTe_{1-y} measured by time-resolved photoluminescence (TRPL).

2. Methods

To codesign Mg_xZn_{1-x}O /CdSe_yTe_{1-y} thin-film solar cells, we fabricated PV device libraries that had orthogonal composition

gradients in CdSe_yTe_{1-y} absorbers and Mg_xZn_{1-x}O contacts using the combinatorial approach. For Mg_xZn_{1-x}O material characterization and growth optimization, thin-film samples with compositional gradients were deposited by combinatorial radio frequency magnetron sputtering from ZnO and Mg targets^[12] on 50 × 50 mm Eagle XG glass substrates. For CdSe_yTe_{1-y} device fabrication, CdSe and CdTe were deposited by sequential thermal evaporation without breaking vacuum, on commercially available 3 × 3" TEC12D glass with bilayer SnO₂ and 120 nm of Mg_xZn_{1-x}O described earlier, with CdSe_yTe_{1-y} gradient orthogonal to the Mg_xZn_{1-x}O gradient. The resulting samples were subject to CdCl₂ and CuCl₂ treatments, followed by thermal evaporation of Au backcontacts. This resulted in combinatorial libraries with 128 Mg_xZn_{1-x}O/CdSe_yTe_{1-y} devices of unique Mg_xZn_{1-x}O and CdSe_yTe_{1-y} composition combinations.

To characterize the resulting Mg_xZn_{1-x}O/CdSe_yTe_{1-y} device libraries, spatially resolved characterization methods were used. For the Mg_xZn_{1-x}O material characterization, each 50 × 50 mm sample library was characterized at 4 × 11 grid of points with spatially resolved measurements of composition using X-Ray fluorescence (XRF), structure using X-Ray diffraction (XRD), and bandgap using optical absorption spectroscopy. The Mg_xZn_{1-x}O/CdSe_yTe_{1-y} device libraries were characterized by current–voltage, external quantum efficiency, time-resolved photoluminescence, and cross-section scanning electron microscopy (SEM). Experimental combinatorial data were processed using our COMBIgor software package^[26] and are available through

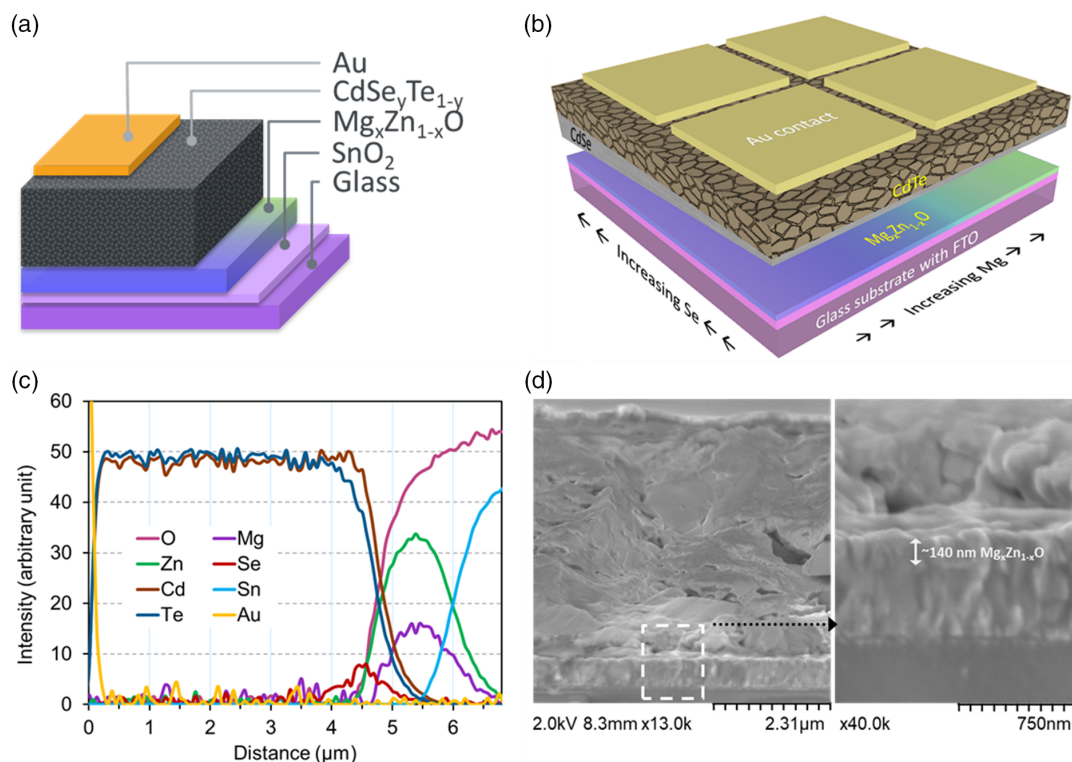


Figure 1. a,b) Device material stack schematics. c) Elemental depth profile from AES in the material stack. d) SEM cross-section image for the Mg_xZn_{1-x}O/CdTe_{1-y}Se_y device.

high-throughput experimental materials database (HTEM DB).^[27] More details about experimental methods are provided in Supplemental Information.

3. Results and Discussion

Figure 1 shows the material stack schematic and cross-sectional SEM. The anneal step to form $\text{CdSe}_y\text{Te}_{1-y}$ from bilayer CdSe/CdTe makes a $\approx 5\ \mu\text{m}$ -thick visually uniform absorber layer. However, the auger electron spectroscopy (AES) elemental depth profile indicates that Se stays within the first micrometer of the absorber. Chlorine was not monitored by AES depth profile. Literatures report that Cl replaces Te and segregates within a few unit cells of the grain boundaries.^[28] In addition, less than a nanometer-thick Cl layers in the form of CdCl_2 accumulate at the front interface, at grain boundaries, and at the back contact.^[29] The $\approx 140\ \text{nm}$ -thick $\text{Mg}_x\text{Zn}_{1-x}\text{O}$ contact layer is clearly identifiable in SEM although the AES profile indicated some level of interdiffusion. Mg composition in $\text{Mg}_x\text{Zn}_{1-x}\text{O}$ measured by XRF varies from $\text{Mg}/(\text{Mg} + \text{Zn}) = 2.0\%$ to 28.5% in the $2'' \times 2''$ glass substrate test libraries (Figure S1, Supporting Information). XRD data reveal ZnO (0002) peaks only for this composition span, with no MgO -related peaks to indicate phase segregation

(Figure S2, Supporting Information). The bandgap determined from optical absorption measurements increases from 3.35 to $4.0\ \text{eV}$ as the Mg composition varies from 2.0% to 28.5% (Figure S3, Supporting Information). Total Se composition in $\text{CdSe}_y\text{Te}_{1-y}$, $\text{Se}/(\text{Se} + \text{Te})$, determined by XRF, ranges from 2.0% to 10.7% (Figure S4, Supporting Information), which is a lower limit for interfacial Se concentration. By examining the long-wavelength QE cutoff (Figure S5, Supporting Information), the optical bandgap for $\text{CdSe}_y\text{Te}_{1-y}$ at the interface can be estimated to range from 1.46 to $1.39\ \text{eV}$. Using literature values,^[30] this results in an estimated $y = 5\text{--}33\%$ composition variation at the $\text{CdSe}_y\text{Te}_{1-y}$ interface. AES depth profiles on select samples are in agreement with the interface Se composition estimated from the QE cutoff, supporting the Se accumulation at the interface due to the solar cell layer stacking sequence where CdSe diffuses into CdTe during CdCl_2 annealing.

Figure 2 maps the current density–voltage (J – V) data for 113 out of the 128 devices as a function of Mg composition in $\text{Mg}_x\text{Zn}_{1-x}\text{O}$ and total Se composition in $\text{CdSe}_y\text{Te}_{1-y}$, while the remaining 15 shunted devices not shown in the plots. The highest V_{OC} is obtained with $3\text{--}8\%$ $\text{Se}/(\text{Se} + \text{Te})$ and $9\text{--}25\%$ $\text{Mg}/(\text{Mg} + \text{Zn})$, while the V_{OC} is lower for low Mg and Se content (Figure 2a). V_{OC} maximum region is more apparent in Figure S6,

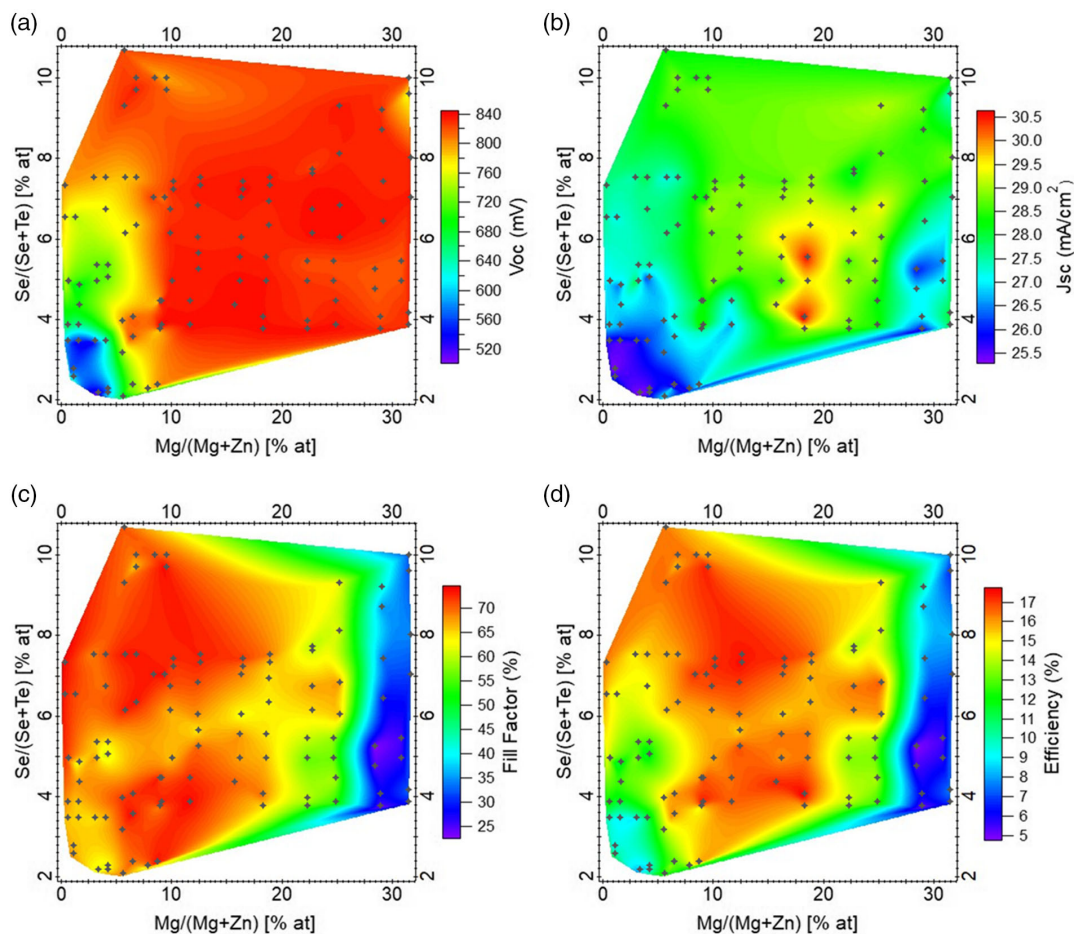


Figure 2. Solar cell device data contour maps: a) V_{OC} , b) J_{SC} , c) fill factor, and d) efficiency for different compositions of $\text{Mg}_x\text{Zn}_{1-x}\text{O}$ and $\text{CdSe}_y\text{Te}_{1-y}$. The black dots are actual device points, while the color map is interpolated.

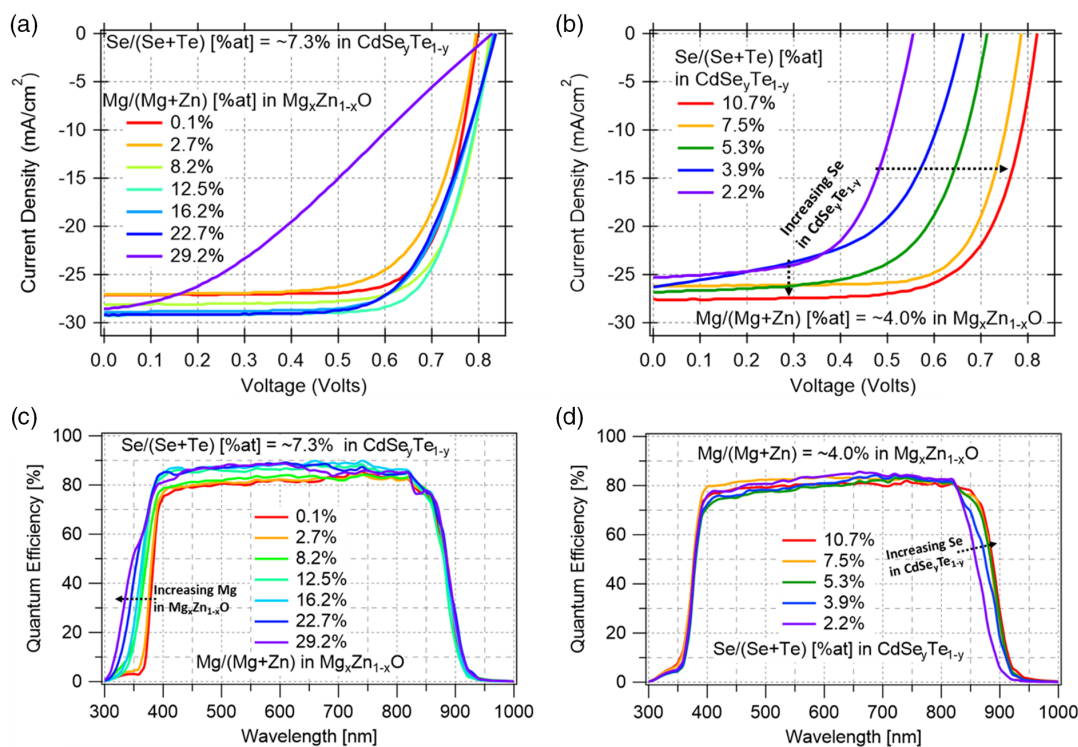


Figure 3. a,b) Current–voltage data and c,d) external quantum efficiency for representative $\text{Mg}_x\text{Zn}_{1-x}\text{O}/\text{CdSe}_y\text{Te}_{1-y}$ solar cells with different $\text{Mg}_x\text{Zn}_{1-x}\text{O}$ and $\text{CdSe}_y\text{Te}_{1-y}$ compositions.

Supporting Information, where the color scale range has been limited. **Figure 3** shows J – V data for representative devices with different $\text{Mg}_x\text{Zn}_{1-x}\text{O}$ and $\text{CdSe}_y\text{Te}_{1-y}$ compositions. For 4% Mg in $\text{Mg}_x\text{Zn}_{1-x}\text{O}$, V_{OC} increases monotonically with increasing Se, despite decreasing bandgap in $\text{CdSe}_y\text{Te}_{1-y}$. This suggests that the increasing V_{OC} is due to better material properties such as interfacial alignment and/or reduced recombination.

The J_{SC} values are more significantly impacted by both compositions, with peak at $\approx 16\%$ Mg and total Se/(Se + Te) of 4–6% (Figure 2b). For a fixed total Se composition of 7.3%, the J_{SC} improves with increasing Mg in $\text{Mg}_x\text{Zn}_{1-x}\text{O}$, due to increased carrier collection at short (blue) wavelengths (Figure 3c) as the bandgap of $\text{Mg}_x\text{Zn}_{1-x}\text{O}$ increases. For fixed Mg composition of 4.0%, J_{SC} improves with increasing Se in $\text{CdSe}_y\text{Te}_{1-y}$ due to bandgap lowering and hence improves carrier collection at longer (red) wavelengths (Figure 3d). The fill factor of the devices is most impacted by $\text{Mg}_x\text{Zn}_{1-x}\text{O}$ composition. Greater Mg results in reduced fill factor, which may be associated with higher $\text{Mg}_x\text{Zn}_{1-x}\text{O}$ film resistivity at high Mg compositions.^[31]

Together, V_{OC} , J_{SC} , and FF are impacted differently by the $\text{Mg}_x\text{Zn}_{1-x}\text{O}$ and $\text{CdSe}_y\text{Te}_{1-y}$ compositions (Figure 2). Although higher compositions are beneficial for J_{SC} , the efficiency is reduced by lower V_{OC} and FF. The result is a complicated efficiency map, with peaks occurring at multiple locations, as shown in Figure 2d and highlighted in Figure S6, Supporting Information. Table S1, Supporting Information lists solar cell parameters for some of the better performing devices. The highest observed V_{OC} was 842 mV, at compositions of $\text{Mg}/(\text{Mg} + \text{Zn}) \approx 9\%$ and total Se/(Se + Te) $\approx 3.8\%$. The highest

observed J_{SC} was 30.6 mA cm^{-2} , which also corresponded to relatively high efficiency of 17.7% despite a modest FF of 69%. This occurred at compositions of $\text{Mg}/(\text{Mg} + \text{Zn}) \approx 18\%$ and total Se/(Se + Te) $\approx 4\%$, with interface Se/(Se + Te) $\approx 23\%$ from AES data. Optimizing device fabrication parameters such as Cl heat treatment and Cu backcontact at the best absorber–contact combination space could lead to further improvement of efficiency above 18%.

Carrier concentration estimated from capacitance–voltage measurements (Figure S7, Supporting Information) indicate a decrease in electron density in 10^{15} cm^{-3} range by $\approx 2\times$ with increasing Se content, consistent with the tendency of II–VI semiconductors with Se or S anions toward n-type doping. For total Se content fixed at $\approx 7.0\%$, increasing Mg increases the depletion width slightly ($\approx 20\%$), though it is difficult to conclusively state that this trend is caused by actual change in carrier density ($\approx 40\%$) rather than variations in the CV measurements. The vertical rise of the carrier concentration near the back of the device is indicative of the full depletion through the entire thickness of the absorber to the back contact. Indeed, the thickness at which the carrier density increases (3.5 – $4.5 \mu\text{m}$) is similar to the nominal absorber thickness ($\approx 5 \mu\text{m}$).

An increase in carrier lifetime is observed with increasing Se in $\text{CdSe}_y\text{Te}_{1-y}$ (Figure 4), which is also reported in other studies.^[32] The interesting observation is the increase in carrier lifetime with increasing Mg in $\text{Mg}_x\text{Zn}_{1-x}\text{O}$, which to our knowledge has not been reported. This can be seen for Se at 7%, where the measured lifetime increases steadily and significantly with increasing Mg content (Figure 4b). Earlier studies have indicated

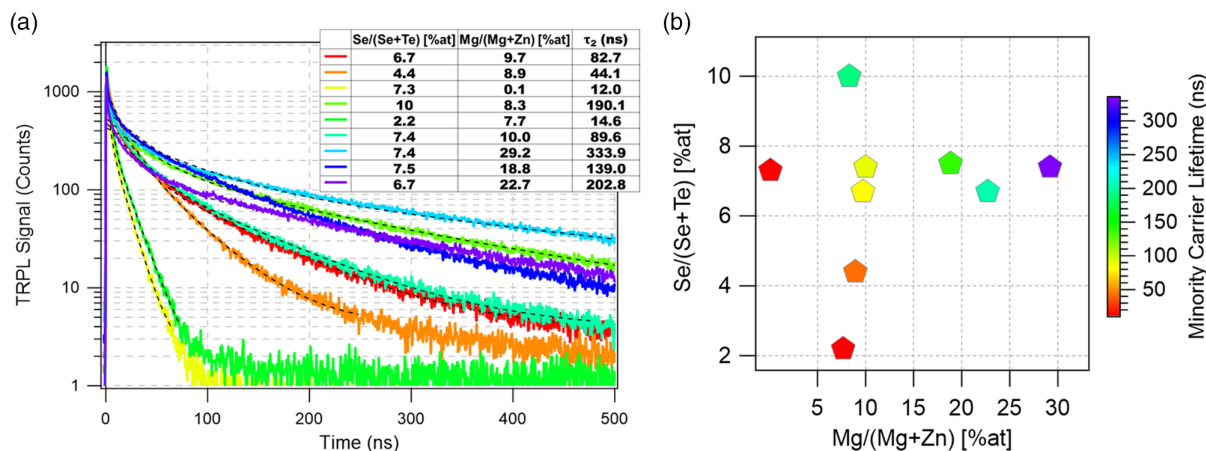


Figure 4. a) One-photon TRPL decay curves for selected samples and b) carrier lifetime data for selected $\text{Mg}_x\text{Zn}_{1-x}\text{O}/\text{CdSe}_y\text{Te}_{1-y}$ devices shown by the color corresponding to the legend on the right.

that the band offset at the $\text{Mg}_x\text{Zn}_{1-x}\text{O}$ and $\text{CdSe}_y\text{Te}_{1-y}$ interface can alter the electron and hole populations at the interface and consequently the recombination kinetics.^[13,33] It is also possible that the interface has fewer defects with increasing Mg content. For example, recent studies have indicated that SnO_2 acts as a catalyst for oxide formation such as tellurates that can enhance passivation.^[34,35] It is possible that Mg similarly alters oxide formation, interfacial chemistry, and passivation.

The increasing lifetime (Figure 4) does correspond to greater V_{OC} as expected (Figure 2), yet the overall device performance falters as Mg atomic content approaches 30% with increased device series resistance and the appearance of barrier effects. Barrier effects and resistance can be the result of overly thick oxide layers and/or poor band offsets. Importantly, these data indicate for the first time the degree to which modifying the buffer composition in and of itself can be a strong proactive approach to manipulate recombination. At the same time, it indicates that this must be done within other constraints such as avoiding overly large barriers that can impede overall performance. Future studies can use combinatorial methods to explore mechanisms and further enhance efficiency by optimizing additional parameters such as Cl heat treatment^[36] and back-contact Cu doping for the best absorber–contact combination space.

4. Conclusions

In summary, CdTe absorber-based solar cell devices were fabricated with orthogonal combinatorial gradients in $\text{Mg}_x\text{Zn}_{1-x}\text{O}$ and $\text{CdSe}_y\text{Te}_{1-y}$ compositions. The performance of more than 100 solar cells fabricated with different $\text{Mg}_x\text{Zn}_{1-x}\text{O}$ and $\text{CdSe}_y\text{Te}_{1-y}$ compositions was compiled, demonstrating systematic changes in V_{OC} , fill factor, and J_{SC} , leading to a complex efficiency contour map. J_{SC} improves with increasing Mg in $\text{Mg}_x\text{Zn}_{1-x}\text{O}$ due to increased transparency, with increasing Se in $\text{CdSe}_y\text{Te}_{1-y}$ due to bandgap lowering, according to the quantum efficiency (QE) measurement results. For the 4% Mg in $\text{Mg}_x\text{Zn}_{1-x}\text{O}$, V_{OC} increases with increasing Se in $\text{CdSe}_y\text{Te}_{1-y}$ despite decreasing bandgap, likely due to better material

properties indicated by increased carrier lifetime. All these results indicate that bandgap engineering can not only influence the light absorption but also lead to long lifetimes and blocking barriers for the photogenerated carriers. Future work can build on this by maintaining properties such as long lifetime while attempting to fix corresponding shortfalls with enhanced emitter doping, manipulating band alignment, and other interfacial engineering.

Supporting Information

Supporting Information is available from the Wiley Online Library or from the author.

Acknowledgements

This work was authored by the National Renewable Energy Laboratory (NREL), operated by Alliance for Sustainable Energy LLC, for the USA. Department of Energy (DOE) under contract no. DE-AC36-08GO28308. Funding was provided by Basic Energy Sciences, as a part of Fuels from Sunlight Hub “Liquid Sunlight Alliance” (absorber and contact co-design); Solar Energy Technologies Office under agreement 34353 (absorber growth); Hydrogen and Fuel Cell Technologies Office (HFTO), as a part of HydroGEN Energy Materials Network (EMN) consortium (contact deposition); and USA. Office of Naval Research under agreement IAG-16-02002 (TRPL characterization). The views expressed in the article do not necessarily represent the views of the DOE or the USA. Government.

Conflict of Interest

The authors declare no conflict of interest.

Data Availability Statement

The data that support the findings of this study are available from the corresponding author upon reasonable request.

Keywords

cadmium telluride, combinatorial, interfaces, magnesium zinc oxide, thin film solar cells

Received: May 25, 2022
Published online: July 20, 2022

- [1] D. Feldman, R. Margolis, Q1/Q2 2020 Solar Industry Update, National Renewable Energy Laboratory, Golden, CO **2020**. <https://doi.org/10.2172/1665843>.
- [2] W. Shockley, H. J. Queisser, *J. Appl. Phys.* **1961**, *32*, 510.
- [3] S.-H. Wei, S. B. Zhang, A. Zunger, *J. Appl. Phys.* **2000**, *87*, 1304.
- [4] A. H. Munshi, J. Kephart, A. Abbas, J. Raguse, J.-N. Beaudry, K. Barth, J. Sites, J. Walls, W. Sampath, *IEEE J. Photovoltaics* **2018**, *8*, 310.
- [5] T. A. M. Fiducia, B. G. Mendis, K. Li, C. R. M. Grovenor, A. H. Munshi, K. Barth, W. S. Sampath, L. D. Wright, A. Abbas, J. W. Bowers, J. M. Walls, *Nat. Energy* **2019**, *4*, 504.
- [6] J. Chantana, T. Kato, H. Sugimoto, T. Minemoto, *ACS Appl. Mater. Interfaces* **2018**, *10*, 11361.
- [7] T. Ablekim, E. Colegrove, W. K. Metzger, *ACS Appl. Energy Mater.* **2018**, *1*, 5135.
- [8] T. Minemoto, T. Negami, S. Nishiwaki, H. Takakura, Y. Hamakawa, *Thin Solid Films* **2000**, *372*, 173.
- [9] A. Ohtomo, M. Kawasaki, T. Koida, K. Masubuchi, H. Koinuma, Y. Sakurai, Y. Yoshida, T. Yasuda, Y. Segawa, *Appl. Phys. Lett.* **1998**, *72*, 2466.
- [10] L. A. Bendersky, I. Takeuchi, K.-S. Chang, W. Yang, S. Hullavarad, R. D. Vispute, *J. Appl. Phys.* **2005**, *98*, 083526.
- [11] S. Lautenschlaeger, J. Sann, P. J. Klar, M. Piechotka, B. K. Meyer, *Phys. Status Solidi B* **2009**, *246*, 383.
- [12] I. S. Khan, C. P. Muzzillo, C. L. Perkins, A. G. Norman, J. L. Young, N. Gaillard, A. Zakutayev, *J. Phys.: Energy* **2021**, *3*, arXiv, 24001.
- [13] T. Ablekim, C. Perkins, X. Zheng, C. Reich, D. Swanson, E. Colegrove, J. N. Duenow, D. Albin, S. Nanayakkara, M. O. Reese, T. Shimpi, W. Sampath, W. K. Metzger, *IEEE J. Photovoltaics* **2019**, *9*, 888.
- [14] M. J. Watts, T.A. M. Fiducia, B. Sanyal, R. Smith, J. M. Walls, P. Goddard, *J. Phys. Condens. Matter* **2020**, *32*, 125702.
- [15] T. Song, A. Kanevce, J. R. Sites, *J. Appl. Phys.* **2016**, *119*, 233104.
- [16] M. L. Green, C. L. Choi, J. R. Hattrick-Simpers, A. M. Joshi, I. Takeuchi, S. C. Barron, E. Campo, T. Chiang, S. Empedocles, J. M. Gregoire, A. G. Kusne, J. Martin, A. Mehta, K. Persson, Z. Trautt, J. Van Duren, A. Zakutayev, *Appl. Phys. Rev.* **2017**, *4*, 011105.
- [17] J. J. Hanak, E. Bykov, H. Elgamel, D. Grecu, J. Putt, N. Reiter, D. Shvydka, R. C. Powell, in *Conf. Rec. IEEE Photovolt. Spec. Conf., IEEE* **2000**, pp. 495–498, <https://doi.org/10.1109/PVSC.2000.915880>.
- [18] H. Liang, W. Liu, S. Lee, J. van Duren, T. Franklin, M. Patten, S. Nijhawan, in *Conf. Record of the IEEE Photovoltaic Specialists Conf., IEEE* **2012**, pp. 3102–3107, <https://doi.org/10.1109/PVSC.2012.6318237>.
- [19] A. D. Collord, H. Xin, H. W. Hillhouse, *IEEE J. Photovoltaics* **2015**, *5*, 288.
- [20] A. W. Welch, L. L. Baranowski, H. Peng, H. Hempel, R. Eichberger, T. Unold, S. Lany, C. Wolden, A. Zakutayev, *Adv. Energy Mater.* **2017**, *7*, 1601935.
- [21] A. Zakutayev, J. D. Perkins, P. A. Parilla, N. E. Widjonarko, A. K. Sigdel, J. J. Berry, D. S. Ginley, *MRS Commun.* **2011**, *1*, 23.
- [22] R. Woods-Robinson, Y. Han, J. S. Mangum, C. L. Melamed, B. P. Gorman, A. Mehta, K. A. Persson, A. Zakutayev, *Matter* **2019**, *1*, 862.
- [23] K. Mokurala, L. L. Baranowski, F. W. De Souza Lucas, S. Siol, M. F. A. M. Van Hest, S. Mallick, P. Bhargava, A. Zakutayev, *ACS Comb. Sci.* **2016**, *18*, 583.
- [24] K. Majhi, L. Bertoluzzi, K. J. Rietwyk, A. Ginsburg, D. A. Keller, P. Lopez-Varo, A. Y. Anderson, J. Bisquert, A. Zaban, *Adv. Mater. Interfaces*, **2016**, *3*, 1500405.
- [25] X. Rodríguez-Martínez, A. Sánchez-Díaz, G. Liu, M. A. Niño, J. Cabanillas-Gonzalez, M. Campoy-Quiles, *Org. Electron.* **2018**, *59*, 288.
- [26] K. R. Talley, S. R. Bauers, C. L. Melamed, M. C. Papac, K. N. Heinselman, I. Khan, D. M. Roberts, V. Jacobson, A. Mis, G. L. Brennecke, J. D. Perkins, A. Zakutayev, *ACS Comb. Sci.* **2019**, *21*, 537.
- [27] A. Zakutayev, N. Wunder, M. Schwarting, J. D. Perkins, R. White, K. Munch, W. Tumas, C. Phillips, *Sci. Data* **2018**, *5*, 1.
- [28] C. Li, Y. Wu, J. Poplawsky, T. J. Pennycook, N. Paudel, W. Yin, S. J. Haigh, M. P. Oxley, A. R. Lupini, M. Al-Jassim, S. J. Pennycook, Y. Yan, *Phys. Rev. Lett.* **2014**, *112*, 156103.
- [29] C. L. Perkins, C. Beall, M. O. Reese, T. M. Barnes, *ACS Appl. Mater. Interfaces* **2017**, *9*, 20561.
- [30] J. Yang, S.-H. Wei, *Chin. Phys. B* **2019**, *28*, 086106.
- [31] P. P. Rajbhandari, A. Bikowski, J. D. Perkins, T. P. Dhakal, A. Zakutayev, *Sol. Energy Mater. Sol. Cells*, **2017**, *159*, 219.
- [32] X. Zheng, D. Kuciauskas, J. Moseley, E. Colegrove, D. S. Albin, H. Moutinho, J. N. Duenow, T. Ablekim, S. P. Harvey, A. Ferguson, W. K. Metzger, *APL Mater.* **2019**, *7*, 071112.
- [33] X. Zheng, E. Colegrove, J. N. Duenow, J. Moseley, W. K. Metzger, *J. Appl. Phys.* **2020**, *128*, 053102.
- [34] C. L. Perkins, D. L. McGott, M. O. Reese, W. K. Metzger, *ACS Appl. Mater. Interfaces* **2019**, *11*, 13003.
- [35] C. L. Perkins, T. Ablekim, T. M. Barnes, D. Kuciauskas, K. G. Lynn, W. Nemeth, M. O. Reese, S. K. Swain, W. K. Metzger, *IEEE J. Photovoltaics* **2018**, *8*, 1858.
- [36] P. Hatton, M. J. Watts, A. Abbas, J. M. Walls, R. Smith, P. Goddard, *Nat. Commun.* **2021**, *12*, 1.